The Effect of a Temperature-Dependent Viscosity on Cooling Droplet-Droplet Collisions

The effect of a temperature-dependent viscosity on cooling droplet-droplet collisions

P.M. Durubal, A. Tavanaei, K.A. Buist, J.A.M. Kuipers, M.W. Baltussen *

Multiphase Reactors Group, Department of Chemical Engineering & Chemistry, Eindhoven University of Technology, P.O. Box 513, 5600 MB Eindhoven, the Netherlands

A R T I C L E   I N F O

A B S T R A C T

A detailed understanding of the collision dynamics of liquid droplets is relevant to natural phenomena and industrial applications. These droplets could experience temperature changes altering their physical properties, which affect the droplet collisions. As viscosity is one of the relevant physical properties, this study focuses on the effect of temperature on viscosity, with an Arrhenius temperature dependence, of collisions of two equal-sized droplets using the Volume of Fluid Method. The results show that the higher temperature of the droplets leads to an effectively lower viscosity, leading to increased interface oscillations. This leads to the onset of separation at lower Weber numbers as expected. The local cooling droplets will create a local viscosity profiles, which results in the formation of a ridge upon combination of droplets. In addition, the collision outcomes sometimes cannot be explained solely on basis of an effective viscosity, undermining the usefulness of existing collision regime maps.

1. Introduction

Understanding of the collision dynamics of liquid droplets is of significant interest for; industrial processes (Brazier-Smith et al., 1972), the transmission of infectious diseases (Dbouk and Drikakis, 2020; Jarvis, 2020), biomedical applications (Koishi et al., 2010), food processing (Finotello et al., 2018b), microfluidics and 3D printing (Baroud et al., 2010; Yin et al., 2021). The outcome of droplet collisions is classified in different regimes such as; coalescence, stretching separation, reflexive separation and bouncing. The collisional outcome depends on the interaction and droplet parameters (the droplet size, the relative velocity of the droplets and the location of the droplets with respect to the collision direction) as well as thermo-physical properties of the system (the densities and viscosities of both the droplets and gas and the surface tension). For example, the temperature history of the droplets leads to altered physical properties resulting in a change in the collision outcome which significantly affects the final droplet size distribution in sprays (Sommerfeld and Pasternak, 2019).

The main physical properties influencing the outcome are surface tension and viscosity, which can be characterized by the Ohnesorge number (Eq. (1)) Gotaas et al. (2007); Jiang et al. (1992).

$$Oh = \frac{\mu_d}{\sqrt{\rho_d d \sigma}} \qquad (1)$$

where μ_d is the viscosity and ρ_d is the droplet density, d is the diameter of the droplet and σ is the surface tension. To determine the effect of the Ohnesorge number on droplet collision outcomes, several studies have been performed using different liquids for the droplets. These show clear shifts in the boundaries of the regimes when the viscosity and the surface tension of the droplets are changed (Al-Dirawi and Bayly, 2020; Baumgartner et al., 2020; Brenn and Kolobaric, 2006; Finotello et al., 2017, 2018b; Gotaas et al., 2007; Jiang et al., 1992; Krishnan and Loth, 2015; Kropotova et al., 2022; Kuschel and Sommerfeld, 2013; Pan et al., 2016; Qian and Law, 1997; Shlegel et al., 2019, 2020; Sommerfeld and Kuschel, 2016; Sun et al., 2013; Zhou et al., 2022a). This research is extended further with the collision of non-identical miscible liquids. It shows that the regime boundaries of the non-identical droplet collisions are in between the regime boundaries of the identical droplet collisions (Al-Dirawi and Bayly, 2020). In addition, the coalescence is generally delayed when two different liquids are used (Focke et al., 2013). For immiscible liquids, however, encapsulation is the main outcome of the collision (Chen and Chen, 2006; Chen et al., 2016). Finally, some research has been performed using non-Newtonian liquids, where the viscosity depends on the local flow characteristics. Comparing the collisions of Newtonian droplets with these non-Newtonian droplets, new regimes appear in the collision diagrams (Finotello et al., 2018a; Focke and Bothe, 2011; França et al., 2022).

---

* Corresponding author.
  E-mail address: m.w.baltussen@tue.nl (M.W. Baltussen).

Besides the local velocity field, the local temperature can also influence the droplet-droplet collision due to a temperature dependence of the viscosity of both the gas and the liquid. Changing the temperature of the surrounding gas leads to changes in the local oscillation dynamics and thereby shifts in the regime boundaries (Islamova et al., 2022; Tkachenko et al., 2021; Volkov et al., 2015). In addition, Volkov et al. (Volkov et al., 2015) found an influence of the initial temperature of the droplets on the shape oscillations.

To extend our understanding of the effect of the variable viscosity on droplet collisions, this research will focus on the effect of temperature dependent viscosity of the liquid on droplet collisions. To effectively study these effects, it is essential to determine the local temperature and viscosity profiles. To obtain these profiles, this study employs a Direct Numerical Simulation (DNS) method. The interested reader is referred to the comprehensive review by Sommerfeld and Kuschel (Sommerfeld and Pasternak, 2019) on the employed numerical methods in the field of binary droplet collisions. Generally, front capturing methods are applied as they are easy to implement and are able to include coalescence (Finotello et al., 2017; Goodarzi et al., 2018; Premnath and Abraham, 2005; Sun et al., 2013; Zhou et al., 2022b). It should be noted however that droplet collisions have also been investigated with a front tracking method (Dai and Schmidt, 2005; Rajkotwala et al., 2020). In this work, we will apply a front capturing method to represent the gas-liquid interface. The method is extended to include the effect of the local temperature profile on the viscosity of the liquid. Using this new method, the effect of an Arrhenius type temperature dependent viscosity on the collision and the collision outcomes of cooling droplets will be determined. This paper is organized as follows: Section 2 discusses the numerical methods and the simulation settings. In Section 3, the results will be presented and discussed. Finally, the conclusions will be given in Section 4.

2. Numerical model

The numerical method applied in this paper is based on the Volume of Fluid (VOF) method developed originally by van Sint Annaland et al. (van Sint Annaland et al., 2005) and improved by Baltussen et al. (Baltussen et al., 2014). The principles of the method will be presented in this section.

2.1. Governing equations and numerical solution

In our model, the continuity, Eq. (2), and the Navier-Stokes equations, Eq. (3), are solved for an incompressible flow using a one-fluid approach.

$$\nabla \cdot \boldsymbol{u} = 0 \tag{2}$$

$$\rho \frac{\partial \boldsymbol{u}}{\partial t} = -\nabla p - \rho \nabla \cdot (\boldsymbol{u}\boldsymbol{u}) - \nabla \cdot \boldsymbol{\tau} + \rho \boldsymbol{g} + \boldsymbol{F}_\sigma \tag{3}$$

where the fluid stress tensor is defined as $\boldsymbol{\tau} = -\mu[\nabla \boldsymbol{u} + (\nabla \boldsymbol{u})^T]$. In Eq. (3), the density and viscosity in each cell are obtained by linear averaging and harmonic averaging with the local fractional amount of liquid (F) according to Eq. (4) and Eq. (5), respectively.

$$\rho = F\rho_l + (1 - F)\rho_g \tag{4}$$

$$\frac{\rho}{\mu} = F\frac{\rho_l}{\mu_l} + (1 - F)\frac{\rho_g}{\mu_g} \tag{5}$$

where subscripts l and g denote liquid (F = 1) and gas (F = 0) phases.

The advection of the gas-liquid interface is governed by the following equation (Eq. (6)):

$$\frac{DF}{Dt} = \frac{\partial F}{\partial t} + \mathbf{u} \cdot \nabla F = 0. \tag{6}$$

In this VOF method, the Piecewise Linear Interface Calculation (PLIC) of Youngs (Youngs, 1982) is employed to advect the F field.

In Eq. (3), F_σ is a source term to account for the surface tension between the two fluids. This volumetric force is calculated by using the Continuum Surface Force (CSF) model of Brackbill et al. (Brackbill et al., 1992) where σ is the surface tension coefficient, κ the local interface curvature, and $\mathbf{n}$ is the interface normal (Eq. (7)).

$$\boldsymbol{F}_\sigma = \sigma \kappa \boldsymbol{n} \tag{7}$$

The curvature is calculated using the Standard Height Function (SHF). To reduce spurious currents, the balanced force algorithm of Francois et al. (Francois et al., 2006) is implemented which ensures that the discretization of the pressure gradient and the force due to surface tension are similar. However, this requires a curvature calculation at the cell faces while the SHF method calculates the curvature at the cell center. To obtain the cell faced curvature, the curvature of both neighboring cells is averaged. For a more extensive description of the curvature calculation, we refer to the work of Patel et al. (2018).

The governing equations are solved on a staggered grid using a two-step projection method. The first step involves the calculation of a tentative velocity field from the decoupled momentum equations where only part of the viscous terms are treated semi-implicitly. The implicit part is chosen such that each velocity component can be solved separately where the (small) explicit part contains among others mixed derivatives. The viscous terms are calculated with a second order central difference scheme whereas the convective terms are calculated using a second order flux delimited Barton scheme. In the second correction step, the final velocities are corrected such that the continuity equation (Eq. (2)) is satisfied. The implicit part of the viscous term and the correction step are solved using an in-house BiCGStab(2) method (Kamath et al., 2020) with the Ifpack2 incomplete LU-decomposition preconditioner of the AMG (Algebraic Multi Grid) preconditioner of the MueLu package of Trilinos (Team, 2020), respectively.

2.2. Thermal energy equation

The temperature field is obtained by solving the following equation for the conservation of energy where T is the temperature and $(-\tau : \nabla \boldsymbol{u})$ is the volumetric rate of viscous energy dissipation.

$$\rho C_p \frac{\partial T}{\partial t} + \rho C_p \nabla \cdot (\boldsymbol{u} T) = \nabla \cdot (k \nabla T) + (-\tau : \nabla \boldsymbol{u}) \tag{8}$$

The local thermal properties, the heat capacity (C_p) and thermal conductivity (k) are determined in Eq. (9) and (10) by simple linear averaging and harmonic averaging, respectively.

$$\rho C_p = F\rho_g C_{p_g} + (1 - F)\rho_l C_{p_l} \tag{9}$$

$$\frac{1}{k} = F\frac{1}{k_g} + (1 - F)\frac{1}{k_l} \tag{10}$$

The volumetric rate of energy dissipation is given by:

$$(-\tau : \nabla \boldsymbol{u}) = \frac{1}{2}\mu \sum_{i=1}^{3}\sum_{j=1}^{3}\left(\frac{\partial u_i}{\partial x_j} + \frac{\partial u_j}{\partial x_i}\right)^2 \tag{11}$$

where the spatial derivatives of the velocity are calculated with second order central difference approximations.

2.3. Simulation settings

In all VOF simulations, two hot droplets of 2 mm equivalent diameter (d) are initialized in air. The computational domain is 5d x 5d x 5d (Fig. 4). On all domain boundaries, free slip boundary conditions are used. The two droplets are placed on the main diagonal of the domain with an initial distance of 0.25d. The air is quiescent while droplets are initialized with a uniform velocity in the opposite directions by assigning the desired velocity to the cells containing the droplet phase. The time step (Δt) is chosen as 1×10^{-6} s, which is well within the Courant–Friedrichs–Lewy (CFL) criterion and the capillary criterion.
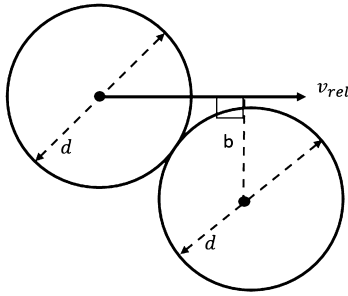
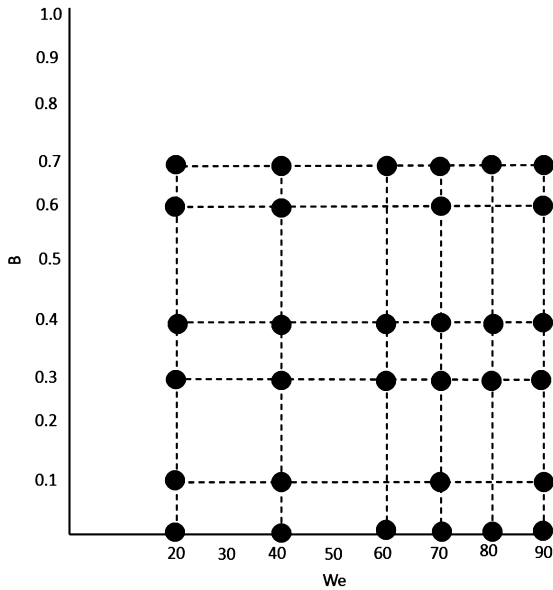**Fig. 1.** Geometric representation of the collision of the binary droplets.

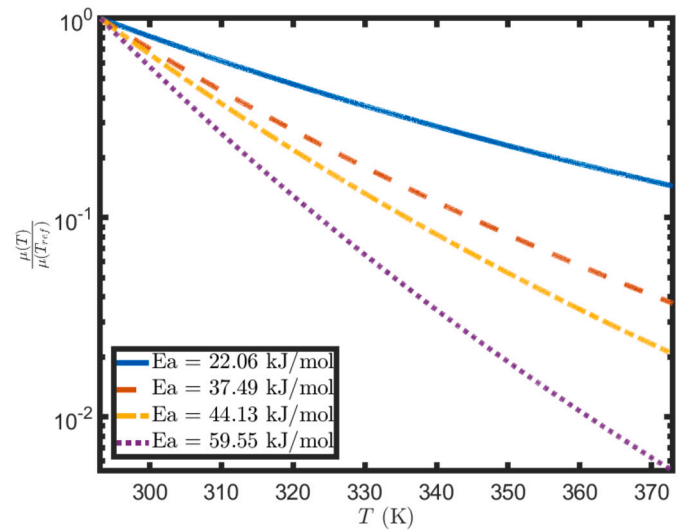**Fig. 2.** The examined cases are based on the We versus B regime map.

Fig. 3. The dependency of the viscosity on temperature for the relevant temperature range.

Table 1
Physical properties of both phases.

Parameter	Liquid phase	Gas phase	Unit
Density	1287	1.25	kg/m^3
Heat capacity	2950	1005	J/kg·K
Thermal conductivity	0.4050	0.02	W/(m·K)
Surface tension	0.077	0.077	N/m

In this study, the effect of the grid size on simulation results was determined using a grid size of 40, 50 and 80 grid cells per diameter for a head-on collision with Weber number (Eq. (12)) equal to 90. As there were no significant differences in the results, the rest of the simulations were performed with a resolution of 40 grid cells per equivalent diameter.

$$We = \frac{\rho_d d v_{rel}^2}{\sigma} \quad (12)$$

Regime maps are used to characterize the droplet-droplet collision outcomes by plotting the non-dimensional impact parameter (B), (Eq. (13)), versus the collision Weber number.

$$B = \frac{b}{d} \quad (13)$$

where b is the distance between the two droplet centers in the plane perpendicular to the relative velocity vector (v_{rel}), and d the diameter of the droplets (Fig. 1). The studied cases are shown in Fig. 2 by black points. A total number of 160 binary droplet collisions have been simulated in this work by varying We between 20 and 90 and B between 0 and 0.7. It should be noted that the regions in which a bouncing collision regime is expected (We below 20 and B above 0.8) are excluded in this study, as the applied Volume of Fluid method is not able to capture the bouncing regime.

The temperature-dependent liquid viscosity is described by an Arrhenius type equation (Eq. (14)) while the air has a viscosity of 1.836×10^{-5} Pa·s.

$$\ln \frac{\mu(T)}{\mu(T_{ref})} = \frac{E_a}{R} \cdot \left(\frac{1}{T} - \frac{1}{T_{ref}} \right) \quad (14)$$

where the reference temperature, T_{ref}, is chosen as 293.15 K, where the viscosity is set to $5.70 \cdot 10^{-2}$ Pa·s. To ensure different ranges of viscosity (0.1, 0.02, 0.01, and 0.002 times $\mu(T_{ref})$), four different values of activation energy (E_a) were used: 22.06, 37.49, 44.13, and 59.55 kJ/mol. The obtained activation energies and associated temperature dependence of the viscosity are consistent with existing fluids, such as glycerol (Peleg, 2018; Telis et al., 2007). The changes of viscosity within the relevant temperature range are shown in Fig. 3.

The other physical and thermophysical properties are given in Table 1 (Martins et al., 2020). Initially, the temperature in the computational domain is 293.15 K while the droplets are at 373.15 K. As the collision times are short compared to the characteristic time for cooling, the main heat transfer resistance is in the gas phase and the overall cooling of the droplet is limited. However, it should be noted that small differences in the temperature in the droplet might lead to significant changes in the local viscosity.

3. Results and discussions

First, the verification of the used Volume of Fluid method is discussed. Next, the binary droplet collisions will be presented in two steps. Firstly, the main effects of a temperature dependent viscosity on the droplet shape will be discussed. Secondly, the combined effects of the temperature dependence and the overall viscosity on conventional regime maps will be analyzed.

3.1. Verification

To investigate the implementation of the surface tension, an air bubble of 3.3 mm is placed in a zero gravity field filled with water. The computational domain is five times the diameter (20 grid cells) in all three dimensions. It is found that the calculated errors in pressure drop over the surface compared to the Laplace pressure (error of 0.54%) and the spurious currents quantified in the Capillary number (Eq. (15), Ca = 8.8×10^{-5}) are comparable to literature values (Baltussen et al., 2014).
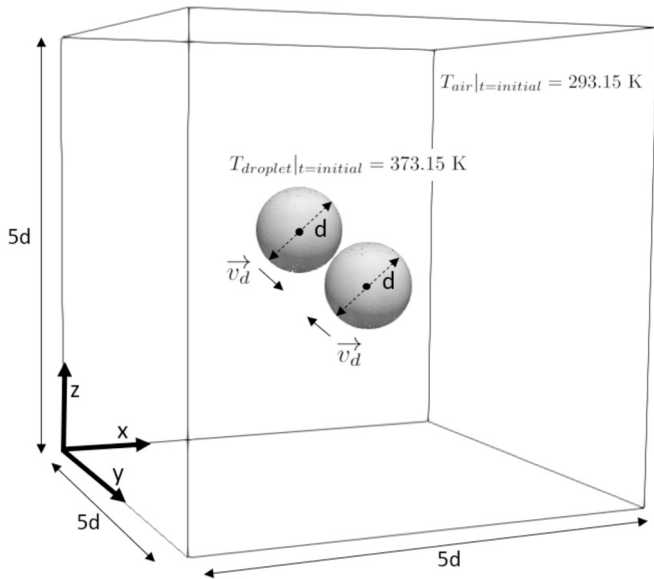
Fig. 4. Position of the droplets inside the computational domain.

Table 2
Simulation settings for the standard advection test.

Parameter	Value	Unit
Bubble diameter	$\frac{1}{6}$	domain size
Bubble placement	$(\frac{1}{2}, \frac{2}{3}, \frac{1}{2})$	domain size
Domain size	(160, 160, 160)	grid cells
Grid size	(0.00625, 0.00625, 0.00625)	m
Time step	2×10^{-3}	s

$$Ca = \frac{\mu_l \mathbf{v}_{max,l}}{\sigma} \tag{15}$$

Secondly, the advection of the gas-liquid interface was tested by advecting a spherical bubble with the velocity field described in Baltussen et al. (2014), which is reversed halfway through the simulation. In this test case (Table 2), the bubble rotates once around the center of the domain. Due to the inversion of the velocity field, the bubble is expected to return to its original position and shape. However, there is a small change in the mass of the bubble and an error in the shape, which is comparable to the literature (the mass error is $\sim 10^{-12}$ and the geometrical errors are $\sim 10^{-2}$ according to the definitions in Baltussen et al. (2014)).

Finally, the implementation of the energy equations was validated using penetration theory. In this simulation, two droplets with a temperature T_d are placed in the air with a lower temperature, T_{air}. The other simulation settings are given in Table 3. The results in Figure 5 show a good comparison with the analytical solution.

3.2. Droplet collisions

There are two main effects of the temperature dependent viscosity on the shape of the collided droplets. These two effects are showcased in all figures of the droplet collisions (Figs. 8, 9, 10, 11, 12, 13 and 15). These figures show the impact and collision outcome of two droplets at several impact parameters and Weber numbers with varying dependency of viscosity on temperature. The collisions are shown in reference to the constant viscosity case, which uses $\mu(T_{ref})$, and one plot of the viscosity distribution of the droplets during impact.

The first effect can be seen in all simulations with a temperature dependent viscosity which shows an increase in the oscillations and elongation of the droplets due to the overall lower viscosity, which is clear in Figs. 8 and 9 for a coalesced droplet pair.

Table 3
Simulation settings and physical properties for the penetration theory test case.

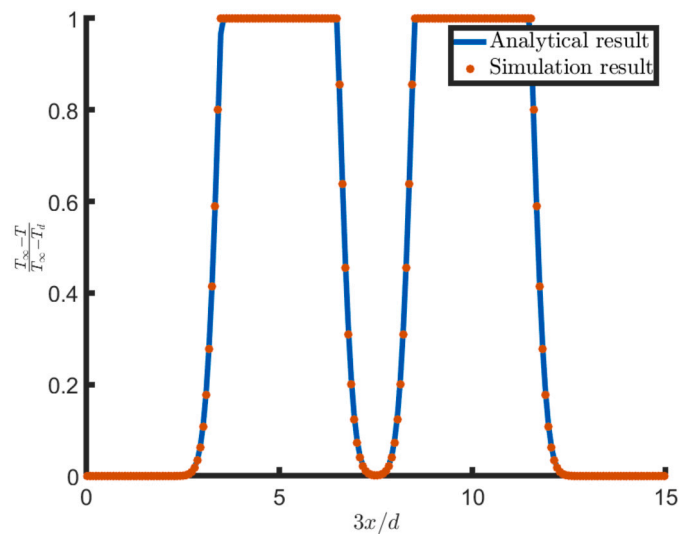| Parameter	Value	Unit
Domain size	(200, 200, 200)	grid cells
Diameter of the droplets	$\frac{1}{5}$	domain size
Position of droplets	$(\frac{1}{3}, \frac{1}{2}, \frac{1}{2})$ and $(\frac{2}{3}, \frac{1}{2}, \frac{1}{2})$	domain size
Grid size	5.0×10^{-5}	m
Time step	1×10^{-6}	s
T_d	373.15	K
T_{air}	293.15	K
ρ_l	997	kg/m^3
ρ_g	1.1845	kg/m^3
C_{p_l}	4181	$J/kg \cdot K$
C_{p_g}	1005	$J/kg \cdot K$
k_l	6.0692	$W/m \cdot K$
k_g	0.0261	$W/m \cdot K$
μ_l	9×10^{-4}	$Pa \cdot s$
μ_g	1.836×10^{-5}	$Pa \cdot s$

Fig. 5. A comparison of the analytical (Bird et al., 2002) and simulation results from the non-dimensional temperature at $1.9 \cdot 10^{-6}$ seconds.
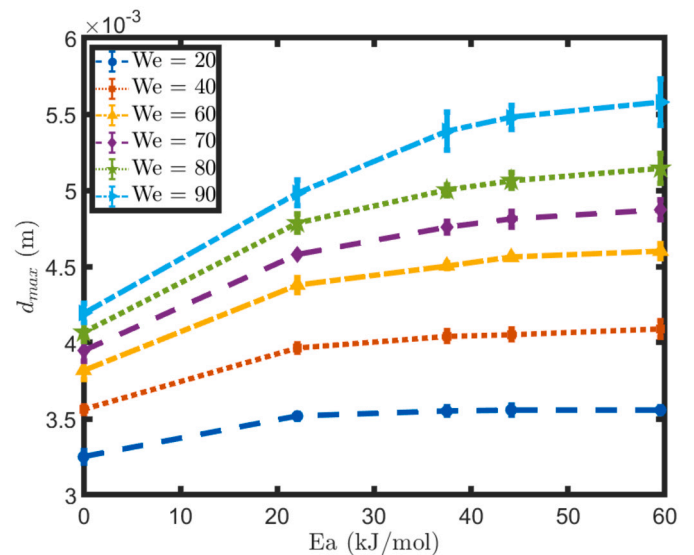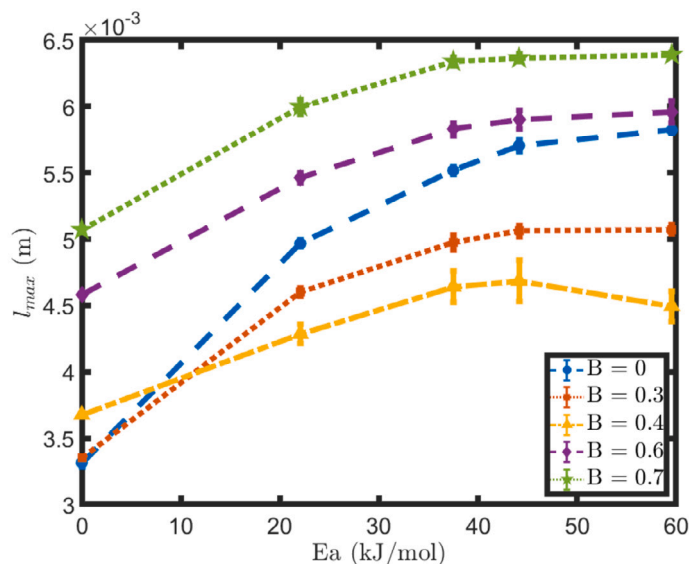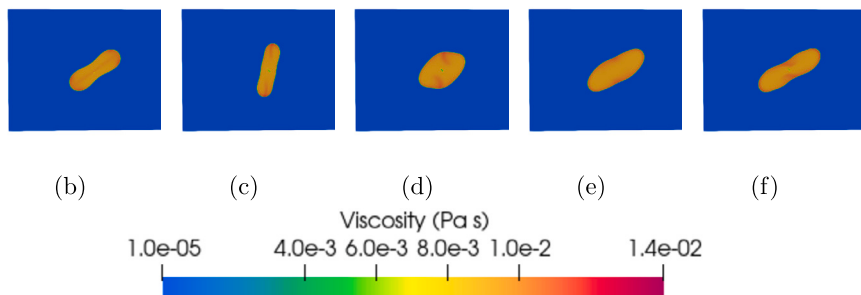

Fig. 6. The maximal diameter of the ring (e.g. Fig. 8 at 4.0 ms to 6.0 ms) formed upon the combination of the droplets for the head-on collisions (B=0). The results with Ea = 0 kJ/mol are the results with constant viscosity ($\mu(T_{ref})$).

(a)

(b)   (c)   (d)   (e)   (f)

Viscosity (Pa s)

Fig. 7. The maximal elongation of the combined droplet pair in Figure a for We = 20. The results with Ea = 0 kJ/mol are the results with constant viscosity ($\mu(T_{ref})$). Figure b-f show the viscosity profiles for all B parameters in Figure a for Ea = 22.06 kJ/mol.

To determine the effect of the temperature dependent viscosity on this elongation, the maximal extension of the ring obtained upon head-on collisions (e.g. Fig. 8 at 4.0 ms to 6.0 ms) can be compared for all cases, which is shown in Fig. 6. The figure clearly shows that the diameter of the ring increases with the Weber number and increased activation energy, which can be directly attributed to the increased kinetic energy and a decrease in the viscous energy dissipation, respectively. It is clear that the extension has an asymptotic behavior towards high activation energies.

Besides the extension of the ring, the effect of the viscosity change can also be compared for the maximal elongation of the complex, which is shown in Fig. 7.a for all collisions with We = 20. The figure shows similar to the extension of the ring that an increase in activation energy leads to more extension of the complex. In the case of a constant viscosity, the extension of the complex increases with B. However, this ordering with B is not obtained in all cases with a temperature dependent viscosity. To explain this difference, the viscosity profiles for Ea = 22.06 kJ/mol are shown in Fig. 7.b-f. These viscosity profiles show that the local viscosity profile changes from aligned with to perpendicular to the main extension direction when changing B from 0 to 0.7. The maximal extension is thus largely dependent on the local viscosity profile and cannot be described by an effective viscosity.

In addition, the overall lower viscosity leads to less dampening of the local fluctuations and might lead to the break up as is clear in case c, d and e in Fig. 8.

Secondly, all cases with a viscosity depending on temperature show the formation of a ridge between two droplets. When two droplets become in contact, a ridge is formed between the two droplet layers due to a relatively high viscosity at the outer surface of the droplets (in Figure 8, 9, 10, and 11 at 1.5 ms, 1.5 ms, 1.0 ms and 1.0 ms, respectively). This increased viscosity is caused by the cooling of the droplets by the surrounding air. The increased viscosity results in a higher energy dissipation resulting in resistance to flow in the contact area of the droplets, leading to a ridge which is resistant to flow. In some cases, a second ridge is observed when the droplets contract or recombine after separation (Figure 8 and Figure 10 at 10 ms and 10.5 ms, respectively). The ridges are more significant when the activation energy is increased. These ridges are never observed in the constant viscosity cases.

3.3. Effects on regime map

As already indicated in the previous section, the changes in the droplet shapes might lead to shifts in the regime maps. This section focuses on the combined effect of the temperature dependence of the viscosity and the overall lower viscosity of the droplets. We will describe the changes with both constant B and We.

At low We and head-on collisions (We = 20 and B = 0, Figure 8), the droplets show a clear ridge formation if a temperature dependent viscosity is used. Afterwards, the combined droplet flattens especially in the region where the droplets initially interact. The thin film will rupture in the simulations, due to the low resolution in the film, leading to a toroidal shape. Although this rupture is not observed experimentally at low Reynolds numbers, contraction of the toroidal shape is similar to experimental work. The contraction in a radial direction results in a spherical shape with distinct dimples in the center. As explained by Qian and Law (1997), this dimple is caused by the conversion of kinetic
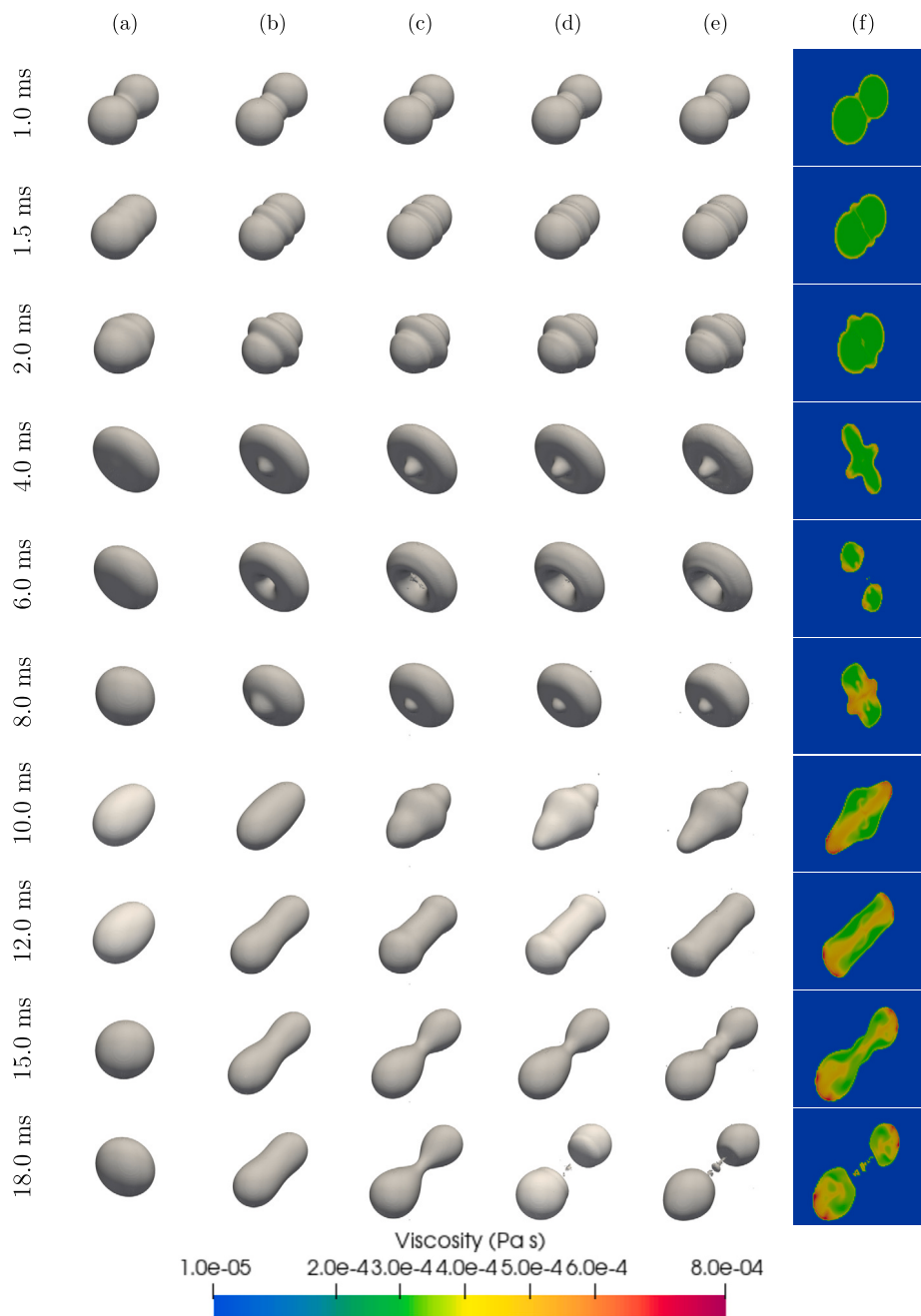
Fig. 8. Collision evolution and rim formations of We = 20, B = 0 for a) constant viscosity ($\mu(T_{ref})$), b) E_a = 22.06 kJ/mol, c) E_a = 37.49 kJ/mol, d) E_a = 44.13 kJ/mol and e) E_a = 59.55 kJ/mol. Figure f) shows the viscosity profile for E_a = 59.55 kJ/mol.

energy to surface energy. Upon recombination, a second ridge appears. After this stage, differences in the droplet outcome start to appear, i.e., the cases with no effect of temperature and the lowest activation energies show coalescence while the case with high activation energies (c, d and e) show separation.

When We is increased (We = 60 and B = 0, Figure 10), similar behavior is found. However, the diameter of the flattened region is increased. At the transition between the flattened region and the rest of the droplet, a neck is formed which results in the formation of a small droplet inside the toroidal droplet. In addition, the droplets show more elongation after the recombination of the droplets resulting in the break-up in three or more droplets, which is known as "end-pinching" (Stone and Leal, 1989) and was also obtained experimentally (Pairam and Fernández-Nieves, 2009), i.e. the obtained results are in the reflexive separation regime (Ashgriz and Poo, 1990; Finotello et

al., 2017; Orme, 1997; Sommerfeld and Pasternak, 2019). Because of the pronounced elongation, the onset of separation occurs at lower activation energies, which was also obtained for different fluids with constant viscosity (Al-Dirawi and Bayly, 2019; Kuschel and Sommerfeld, 2013).

Increasing the We number even further (We = 90) as in Fig. 13, the flattened region extends further resulting in break-up of the toroidal structure in multiple droplets. The changes of break-up are enhanced at the higher activation energies as the interface oscillations are increased. This particular shape is also found by numerically by Rajkotwala et al. (Rajkotwala et al., 2020) and the oscillations in the rim are also observed experimentally by Finotello et al. (Finotello et al., 2018a; Zhou et al., 2022a). Comparing Figures 8, 10 and 13, it is clear that generally the regime boundaries are shifted towards lower We as the interface oscillations promote the break-up of the droplets when the viscosity is
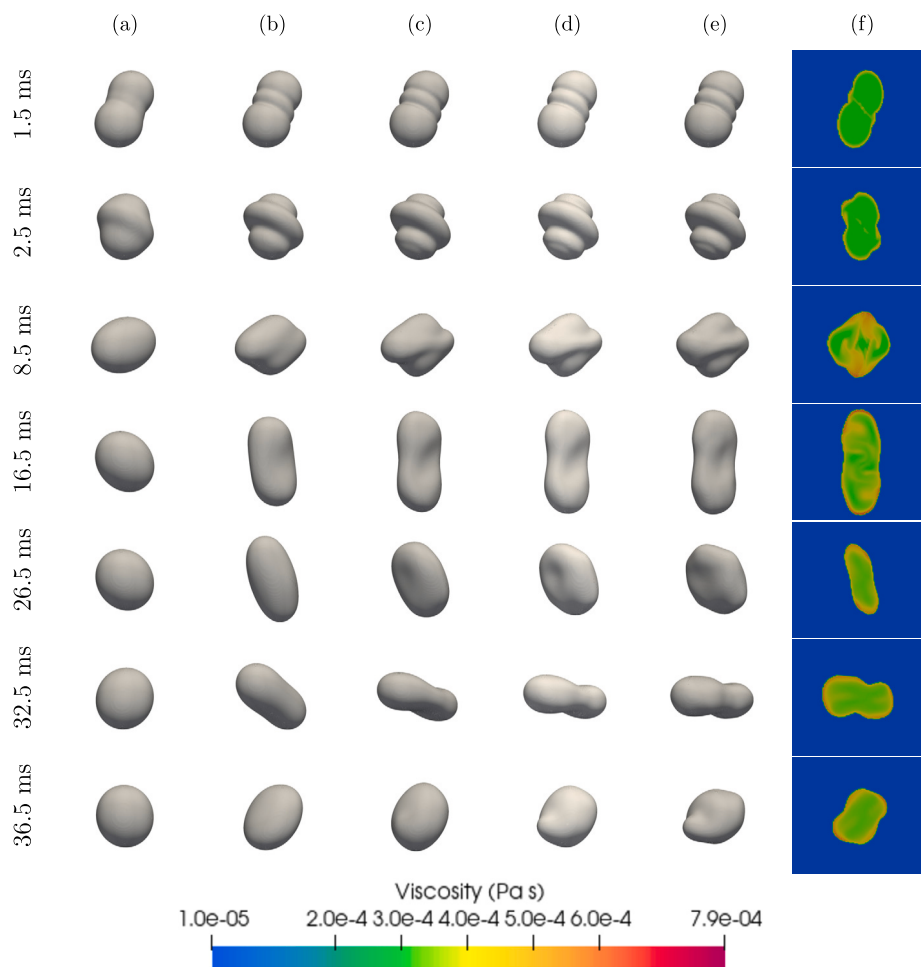
Fig. 9. Collision evolution of We = 20, B = 0.3 for a) constant viscosity ($\mu(T_{ref})$), b) E_a = 22.06 kJ/mol, c) E_a = 37.49 kJ/mol, d) E_a = 44.13 kJ/mol and e) E_a = 59.55 kJ/mol. Figure f) shows the viscosity profile for E_a = 59.55 kJ/mol.

temperature dependent. However, in the case with E_a = 59.55 kJ/mol (Fig. 13 e) coalescence was obtained while separation is expected. When examining the local viscosity profiles in Fig. 14, the case with separation (E_a = 44.13 kJ/mol) shows that the viscosity profile is aligned with the main direction of flow when the separation occurs, while in case with coalescence (E_a = 59.55 kJ/mol) the profile is perpendicular to the main flow direction. These differences are caused by the higher oscillations for the case with higher activation energy (E_a = 55.95 kJ/mol, Fig. 13), which results in more mixing of the liquid and a higher dissipation rate, leading to coalescence.

When changing the impact parameter direction to B = 0.3, three different collision regimes are encountered at the considered We: coalescence and stretching separation. At low We (We = 20 and B = 0.3, Figure 9) coalescence is expected, which is also obtained for all cases although an increase in oscillations is observed for the cases with a temperature dependent viscosity. Increasing We to 60 (Fig. 11), coalescence is still expected when the viscosity is constant. However, the increase in the oscillations observed for the case with the highest activation energy (Fig. 11 e) leads to the break-up of the droplets, i.e. stretching separation is obtained instead of coalescence. This earlier onset of the stretching separation is also expected as an effective lower viscosity is obtained in the droplets, which leads to less viscous energy dissipation and thus more kinetic energy for separation of the droplets (Finotello et al., 2017; Qian and Law, 1997). At the highest We (We = 90, Figure-15), a film is formed after the initial stage of interaction similar to head on collisions. However, the breakage of the film is not symmetric and only in the direction perpendicular to the main interaction direction. In ad-

dition, the recombined droplets show a very distinct profile when a temperature dependent viscosity profile is used. This profile leads to the separation in three droplets. Thus, it can be concluded that in this case the boundaries of the regime are also shifted to lower We in this figure. It should be noted that the physical relevance of the small scale structures is minor as these structures are not resolved ($d_{structure}$ ~ grid size).

When comparing the results at different B (We = 60, Figure 10, 11 and 12), coalescence is less prominent with increased activation energy. The increase of the activation energy leads to more interface oscillations due to the overall lower viscosity in the simulations. The enhanced interface oscillations result in more break-up effectively decreasing the region in which coalescence occurs in the collision diagram. It should be noted that in cases with We = 60 and B > 0.4, there are no effects observed with respect to regime changes as all these interactions already result in separation with constant viscosity.

In general, the simulational results show that the usage of a temperature dependent viscosity results in a shift of the regime boundaries. This is very similar to the results obtained with different liquids, where a decrease in the Ohnesorge number results in a shift of the regime boundaries to lower We, i.e. separation occurs at lower We (Finotello et al., 2017). However, the head-on collisions at We = 90, Fig. 13 in combination with Fig. 14, showed that the local viscosity profile affects the collision outcome. Therefore, the differences in collision outcomes cannot be solely attributed to a decrease in the effective viscosity profile.
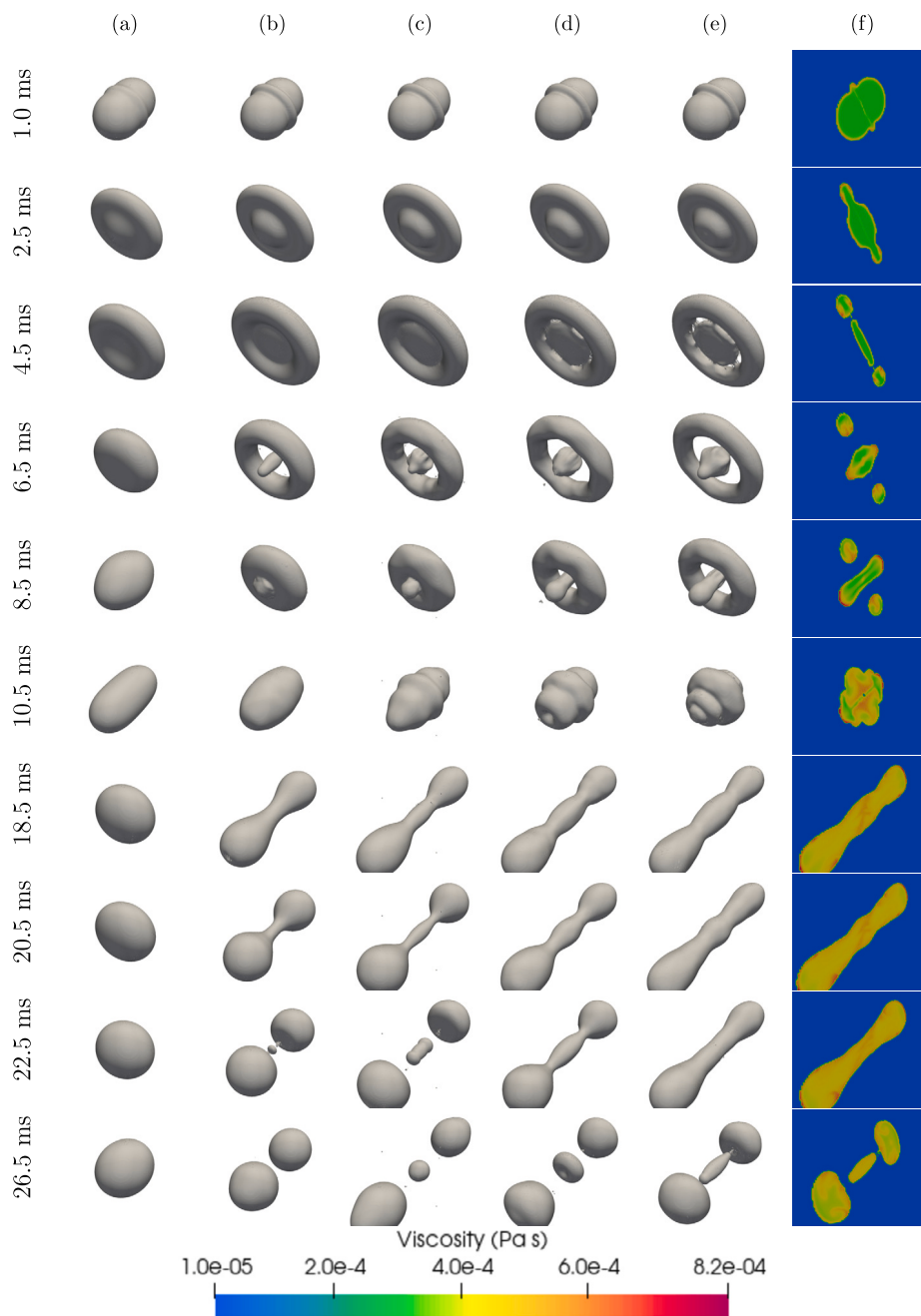
Fig. 10. Collision evolution of We = 60, B = 0.0 for a) constant viscosity ($\mu(T_{ref})$), b) E_a = 22.06 kJ/mol, c) E_a = 37.49 kJ/mol, d) E_a = 44.13 kJ/mol and e) E_a = 59.55 kJ/mol. Figure f) shows the viscosity profile for E_a = 59.55 kJ/mol.

4. Conclusions

In this work, the effect of temperature-dependent viscosity with binary equal-sized droplet collisions is studied numerically using a Volume of Fluid method. The viscosity is dependent on the temperature with an Arrhenius type equation. After verification, the effect of the temperature dependence on collisions of cooling droplets was studied for different Weber numbers (ranging from 20 to 90) and impact parameters B (varying from 0 to 0.7). As the droplets are initially at a higher temperature, the temperature dependent viscosity results in a relatively lower effective viscosity in the droplets than the reference results with a constant viscosity. This results in more oscillations and elongations when the droplets interact. Besides the overall effectively lower viscosity, the cooling of the droplets leads to local viscosity profiles. Just before the collisions, the skin of the droplets is cooled, which results in

a higher viscosity of this skin. Due to the higher viscous dissipation at the point of interaction, a ridge is formed between the original droplets. This ridge formation is also observed when there is a secondary combination of the droplets. In general, the temperature dependency leads to similar changes in the regime map as a decrease in the Ohnesorge number, i.e. the regime boundaries are shifted to lower Weber numbers. This is expected as a decrease in the viscosity leads to less viscous energy dissipation and thus more surface energy and kinetic energy. It should however be noted that the local gradients in the viscosity profile might lead to unexpected collision outcomes. Therefore, the regime maps for cooling droplets with a temperature dependent viscosity cannot be created on the basis of an effective viscosity when a droplet with a temperature dependent viscosity is used. As this study is limited to a temperature difference of 80K between the droplets and their surrounding medium, we recommend extending the research with more
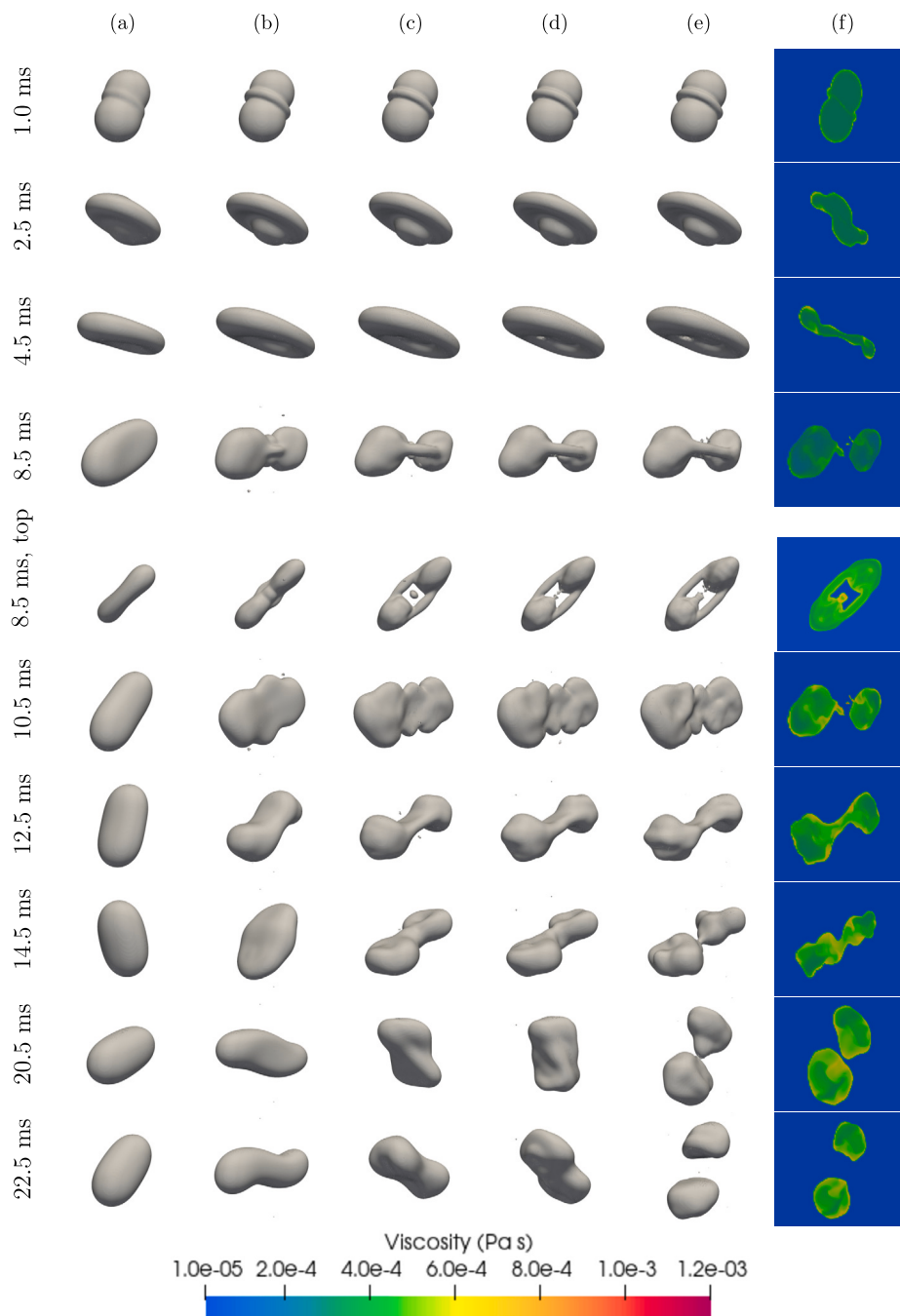
Fig. 11. Collision evolution of We = 60, B = 0.3 for a) constant viscosity ($\mu(T_{ref})$), b) E_a = 22.06 kJ/mol, c) E_a = 37.49 kJ/mol, d) E_a = 44.13 kJ/mol and e) E_a = 59.55 kJ/mol. Figure f) shows the viscosity profile for E_a = 59.55 kJ/mol.

temperature differences. An initial study showed that a decrease in the temperature difference to 40K shows less pronounced differences with the constant viscosity case. It would also be interesting to look at the heating of droplets instead of the cooling. In addition, the physical properties of the liquid and the gas, except for the temperature dependent viscosity, have not been varied in this work. It would be interesting to see the effect of the Biot number and Prandtl number on the effect of the temperature dependent viscosity. It should be noted that an increase in the Biot number might lead to a dependency on the initial temperature profile in the droplets. This should be taken into account in further research. Finally, the surface tension was considered independent of temperature in this research. However, changes in the surface tension with temperature will lead to thermal Marangoni effects.

Declaration of competing interest

The authors declare that they have no known competing financial interests or personal relationships that could have appeared to influence the work reported in this paper.

Data availability

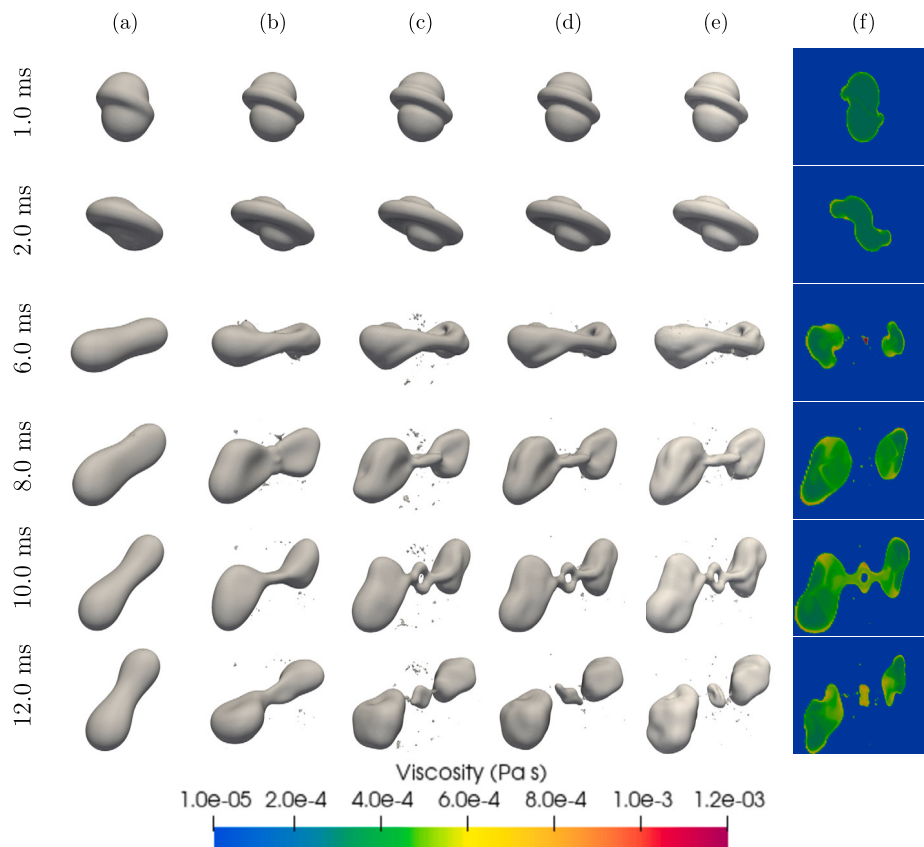Data will be made available on request.

Acknowledgements

Fig. 12. Collision evolution of We = 60, B = 0.4 for a) constant viscosity ($\mu(T_{ref})$), b) E_a = 22.06 kJ/mol, c) E_a = 37.49 kJ/mol, d) E_a = 44.13 kJ/mol and e) E_a = 59.55 kJ/mol. Figure f) shows the viscosity profile for E_a = 59.55 kJ/mol.

Fig. 13. Collision evolution of We = 90, B = 0.0 for a) constant viscosity ($\mu(T_{ref})$), b) E_a = 22.06 kJ/mol, c) E_a = 37.49 kJ/mol, d) E_a = 44.13 kJ/mol and e) E_a = 59.55 kJ/mol. Figure f) shows the viscosity profile for E_a = 59.55 kJ/mol.

Fig. 14. Local viscosity profile of the droplets for We = 90, B = 0.0 for a) E_a = 44.13 kJ/mol and b) E_a = 59.55 kJ/mol.
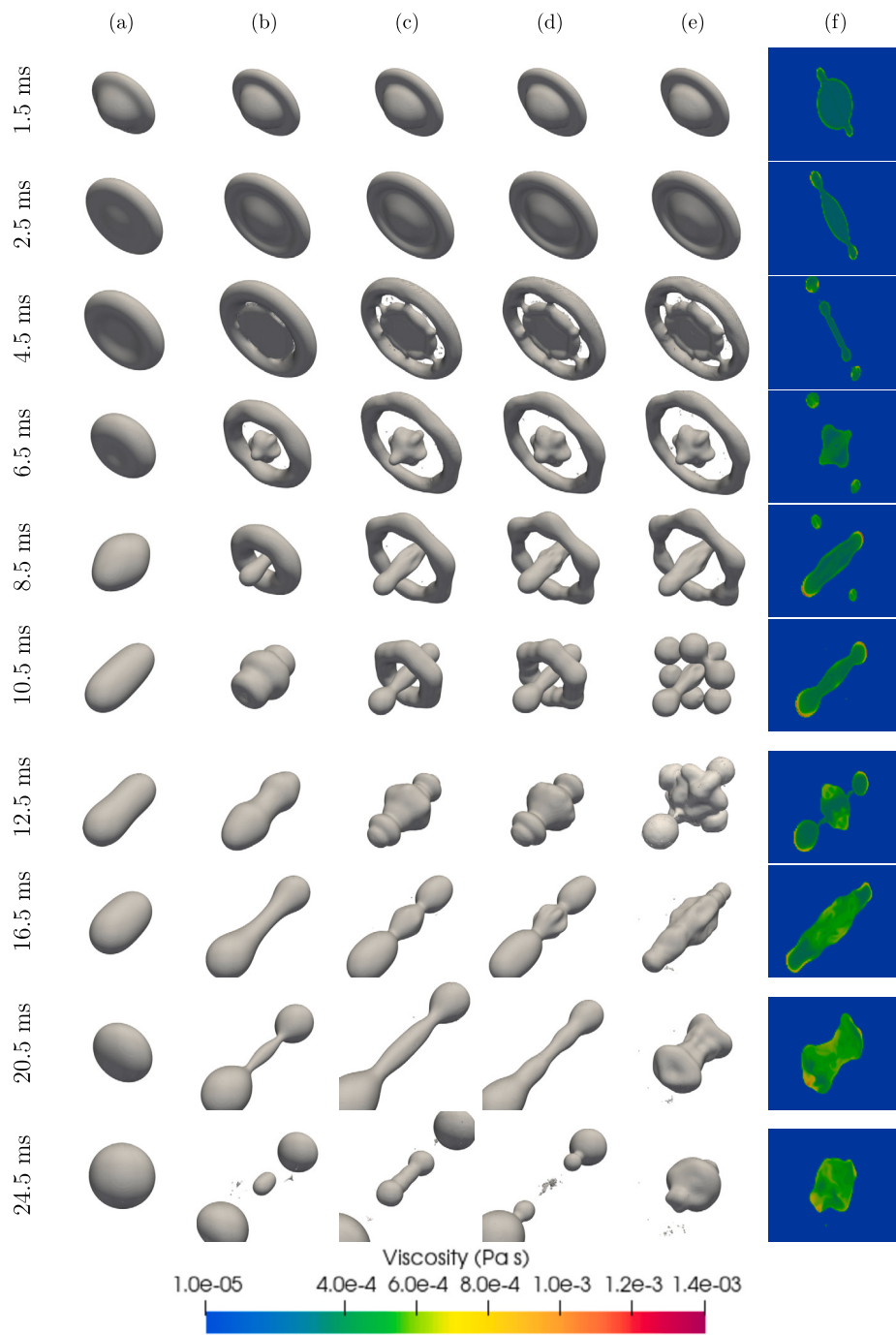
Fig. 15. Collision evolution of We = 90, B = 0.3 for a) constant viscosity ($\mu(T_{ref})$), b) E_a = 22.06 kJ/mol, c) E_a = 37.49 kJ/mol, d) E_a = 44.13 kJ/mol and e) E_a = 59.55 kJ/mol. Figure f) shows the viscosity profile for E_a = 59.55 kJ/mol.
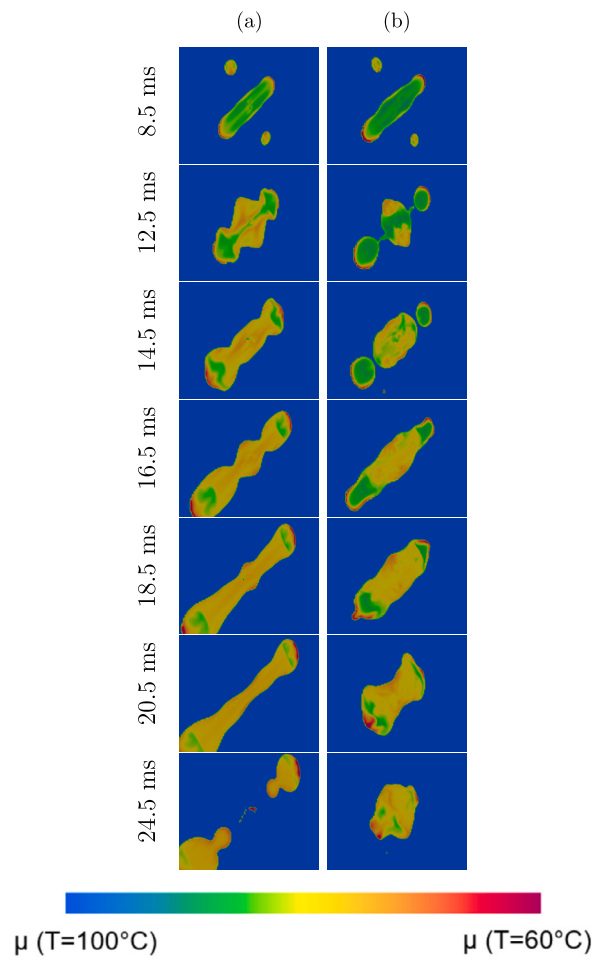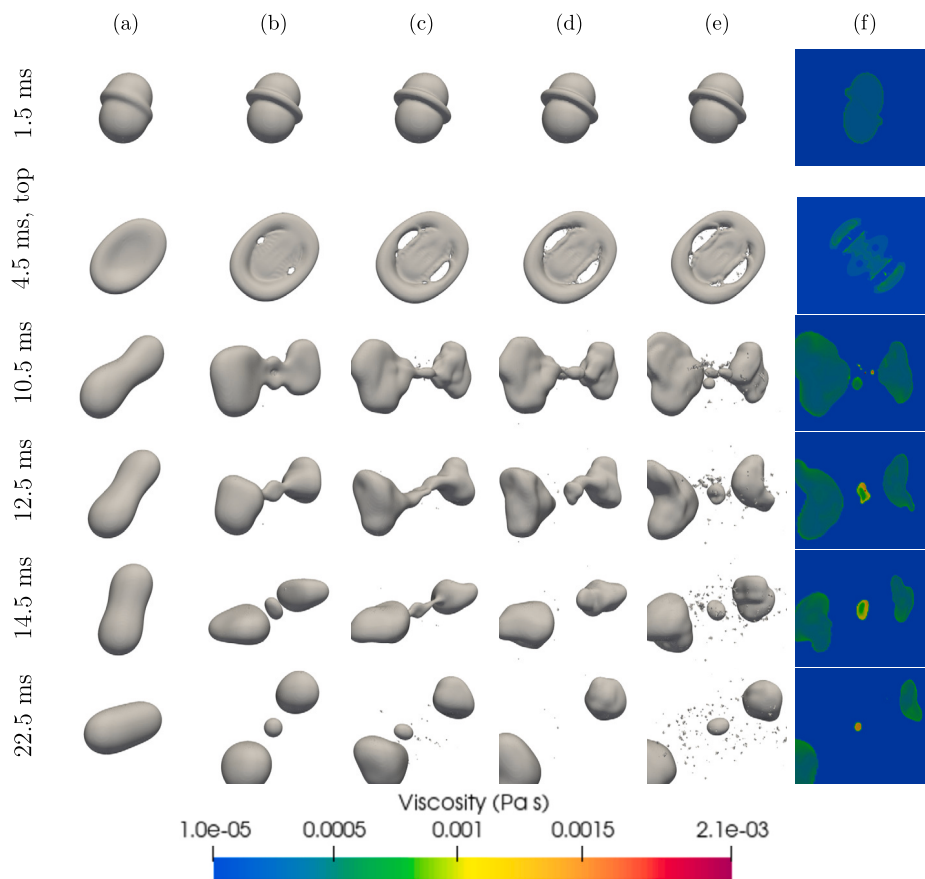
References

Al-Dirawi, K.H., Bayly, A.E., 2019. A new model for the bouncing regime boundary in binary droplet collisions. Phys. Fluids 31 (2).

Al-Dirawi, K.H., Bayly, A.E., 2020. An experimental study of binary collisions of miscible droplets with non-identical viscosities. Exp. Fluids 61 (2), 1–22.

Ashgriz, N., Poo, J.Y., 1990. Coalescence and separation in binary collisions of liquid drops. J. Fluid Mech. 221, 183–204.

Baltussen, M.W., Kuipers, J.A.M., Deen, N.G., 2014. A critical comparison of surface tension models for the volume of fluid method. Chem. Eng. Sci. 109, 65–74.

Baroud, C.N., Gallaire, F., Dangla, R., 2010. Dynamics of microfluidic droplets. Lab Chip 10 (16), 2032–2045.

Baumgartner, D., Brenn, G., Planchette, C., 2020. Effects of viscosity on liquid structures produced by in-air microfluidics. Phys. Rev. Fluids 5 (10), 103602.

Bird, R.B., Stewart, W.E., Lightfoot, E.N., 2002. Transport Phenomena. J. Wiley.

Brackbill, J.U., Kothe, D.B., Zemach, C., 1992. A continuum method for modeling surface tension. J. Comput. Phys. 100 (2), 335–354.

Brazier-Smith, P.R., Jennings, S.G., Latham, J., 1972. The interaction of falling water drops: coalescence. Proc. R. Soc. Lond. Ser. A, Math. Phys. Sci. 326 (1566), 393–408.

Brenn, G., Kolobaric, V., 2006. Satellite droplet formation by unstable binary drop collisions. Phys. Fluids 18 (8), 087101.

Chen, R.-H., Chen, C.-T., 2006. Collision between immiscible drops with large surface tension difference: diesel oil and water. Exp. Fluids 41 (3), 453–461.

Chen, R.-H., Wang, W.-C., Chen, Y.-W., 2016. Like-drop collisions of biodiesel and emulsion diesel. Eur. J. Mech. B, Fluids 60, 62–69.

Dai, M., Schmidt, D.P., 2005. Numerical simulation of head-on droplet collision: effect of viscosity on maximum deformation. Phys. Fluids 17 (4), 041701.

Dbouk, T., Drikakis, D., 2020. On coughing and airborne droplet transmission to humans. Phys. Fluids 32 (5), 053310.

Finotello, G., Padding, J.T., Deen, N.G., Jongsma, A., Innings, F., Kuipers, J.A.M., 2017. Effect of viscosity on droplet-droplet collisional interaction. Phys. Fluids 29 (6), 067102.

Finotello, G., De, S., Vrouwenvelder, J.C., Padding, J.T., Buist, K.A., Jongsma, A., Innings, F., Kuipers, J.A.M., 2018a. Experimental investigation of non-newtonian droplet collisions: the role of extensional viscosity. Exp. Fluids 59 (7), 1–16.

Finotello, G., Kooiman, R.F., Padding, J.T., Buist, K.A., Jongsma, A., Innings, F., Kuipers, J.A.M., 2018b. The dynamics of milk droplet–droplet collisions. Exp. Fluids 59, 1–19.

Focke, C., Bothe, D., 2011. Computational analysis of binary collisions of shear-thinning droplets. J. Non-Newton. Fluid Mech. 166 (14–15), 799–810.

Focke, C., Kuschel, M., Sommerfeld, M., Bothe, D., 2013. Collision between high and low viscosity droplets: direct numerical simulations and experiments. Int. J. Multiph. Flow 56, 81–92.

França, H.L., Oishi, C.M., Thompson, R.L., 2022. Numerical investigation of shear-thinning and viscoelastic binary droplet collision. J. Non-Newton. Fluid Mech. 302, 104750.

Francois, M.M., Cummins, S.J., Dendy, E.D., Kothe, D.B., Sicilian, J.M., Williams, M.W., 2006. A balanced-force algorithm for continuous and sharp interfacial surface tension models within a volume tracking framework. J. Comput. Phys. 213, 141–173.

Goodarzi, Z., Ahmadi Nadooshan, A., Bayareh, M., 2018. Numerical investigation of off-centre binary collision of droplets in a horizontal channel. J. Braz. Soc. Mech. Sci. Eng. 40 (3), 1–10.

Gotaas, C., Havelka, P., Jakobsen, H.A., Svendsen, H.F., Hase, M., Roth, N., Weigand, B., 2007. Effect of viscosity on droplet-droplet collision outcome: experimental study and numerical comparison. Phys. Fluids 19 (10), 102106.

Islamova, A., Kropotova, S., Shlegel, N., Strizhak, P., 2022. The collisions of droplets and particles at the different initial temperatures. Int. J. Heat Mass Transf. 196, 123301.

Jarvis, M.C., 2020. Aerosol transmission of Sars-cov-2: physical principles and implications. Front. Public Health 8, 590041.

Jiang, Y.J., Umemura, A., Law, C.K., 1992. An experimental investigation on the collision behaviour of hydrocarbon droplets. J. Fluid Mech. 234, 171–190.

Kamath, S., Masterov, M.V., Padding, J.T., Buist, K.A., Baltussen, M.W., Kuipers, J.A.M., 2020. Parallelization of a stochastic euler-lagrange model applied to large scale dense bubbly flows. J. Comput. Phys. X (8), 100058.

Koishi, T., Yasuoka, K., Zeng, X.C., Fujikawa, S., 2010. Molecular dynamics simulations of urea–water binary droplets on flat and pillared hydrophobic surfaces. Faraday Discuss. 146, 185–193.

Krishnan, K.G., Loth, E., 2015. Effects of gas and droplet characteristics on drop-drop collision outcome regimes. Int. J. Multiph. Flow 77, 171–186.

Kropotova, S., Tkachenko, P., Strizhak, P., 2022. The effect of impurities on water droplet collision regimes and behavior. Microgravity Sci. Technol. 34 (4), 54.

Kuschel, M., Sommerfeld, M., 2013. Investigation of droplet collisions for solutions with different solids content. Exp. Fluids 54, 1–17.

Martins, M.J.N., Guimarães, B., Polachini, T.C., Telis-Romero, J., 2020. Thermophysical properties of carbohydrate solutions: correlation between thermal and transport properties. J. Food Process Eng. 43 (9), e13483.

Orme, M., 1997. Experiments on droplet collisions, bounce, coalescence and disruption. Prog. Energy Combust. Sci. 23 (1), 65–79.

Pairam, E., Fernández-Nieves, A., 2009. Generation and stability of toroidal droplets in a viscous liquid. Phys. Rev. Lett. 102 (23), 234501.

Pan, K.-L., Tseng, Y.-H., Chen, J.-C., Huang, K.-L., Wang, C.-H., Lai, M.-C., 2016. Controlling droplet bouncing and coalescence with surfactant. J. Fluid Mech. 799, 603–636.

Patel, H.V., Kuipers, J.A.M., Peters, E.A.J.F., 2018. Computing interface curvature from volume fractions: a hybrid approach. Comput. Fluids 161, 74–88.

Peleg, M., 2018. Temperature–viscosity models reassessed. Crit. Rev. Food Sci. Nutr. 58 (15), 2663–2672.

Premnath, K.N., Abraham, J., 2005. Simulations of binary drop collisions with a multiple-relaxation-time lattice-boltzmann model. Phys. Fluids 17 (12), 122105.

Qian, J., Law, C.K., 1997. Regimes of coalescence and separation in droplet collision. J. Fluid Mech. 331, 59–80.

Rajkotwala, A.H., Gelissen, E.J., Peters, E.A.J.F., Baltussen, M.W., van der Geld, C.W.M., Kuerten, J.G.M., Kuipers, J.A.M., 2020. Comparison of the local front reconstruction method with a diffuse interface model for the modeling of droplet collisions. Chem. Eng. Sci. X (7), 100066.

Shlegel, N., Strizhak, P., Volkov, R., 2019. Collision behavior of heterogeneous liquid droplets. Microgravity Sci. Technol. 31, 487–503.

Shlegel, N.E., Tkachenko, P.P., Strizhak, P.A., 2020. Influence of viscosity, surface and interfacial tensions on the liquid droplet collisions. Chem. Eng. Sci. 220, 115639.

Sommerfeld, M., Kuschel, M., 2016. Modelling droplet collision outcomes for different substances and viscosities. Exp. Fluids 57 (12), 1–23.

Sommerfeld, M., Pasternak, L., 2019. Advances in modelling of binary droplet collision outcomes in sprays: a review of available knowledge. Int. J. Multiph. Flow 117, 182–205.

Stone, H.A., Leal, L.G., 1989. Relaxation and breakup of an initially extended drop in an otherwise quiescent fluid. J. Fluid Mech. 198, 399–427.

Sun, K., Jia, M., Wang, T., 2013. Numerical investigation of head-on droplet collision with lattice boltzmann method. Int. J. Heat Mass Transf. 58 (1–2), 260–275.

Team, T.P., 2020. The trilinos project website. https://trilinos.github.io.

Telis, V.R.N., Telis-Romero, J., Mazzotti, H.B., Gabas, A.L., 2007. Viscosity of aqueous carbohydrate solutions at different temperatures and concentrations. Int. J. Food Prop. 10 (1), 185–195.

Tkachenko, P., Shlegel, N., Strizhak, P., 2021. Collisions of water droplets in the high-temperature air. Int. J. Heat Mass Transf. 170, 121011.

van Sint Annaland, M., Deen, N.G., Kuipers, J.A.M., 2005. Numerical simulation of gas bubbles behaviour using a three-dimensional volume of fluid method. Chem. Eng. Sci. 60 (11), 2999–3011.

Volkov, R.S., Kuznetsov, G.V., Strizhak, P.A., 2015. Water droplet deformation in gas stream: impact of temperature difference between liquid and gas. Int. J. Heat Mass Transf. 85, 1–11.

Yin, Z., Su, R., Zhang, W., Zhang, C., Xu, H., Hu, H., Zhang, Z., Huang, B., Liu, F., 2021. Binary collisions of equal-sized water nanodroplets: molecular dynamics simulations. Comput. Mater. Sci. 200, 110774.

Youngs, D.L., 1982. Time-Dependent Multi-Material Flow with Large Fluid Distortion. Numerical Methods for Fluid Dynamics.

Zhou, D., Liu, X., Yang, S., Hou, Y., Zhong, X., 2022a. Intense deformation and fragmentation of two droplet collision at high weber numbers. Colloids Surf. A, Physicochem. Eng. Asp. 655, 130171.

Zhou, D., Liu, X., Yang, S., Hou, Y., Zhong, X., 2022b. Collision dynamics of two liquid nitrogen droplets under a low-temperature condition. Cryogenics 124, 103478.